Preprints of the 21st IFAC World Congress (Virtual)
Berlin, Germany, July 12-17, 2020

Rigid-Joint-Model Feedforward with Elastic-Joint-Model Feedback for Motion Control of a 6-DOF Industrial Robot

Junji Oaki *

* *Corporate Research & Development Center, Toshiba Corporation Kawasaki, Japan (e-mail: junji.ooaki@toshiba.co.jp).*

Abstract: This paper presents a fast and exact trajectory control scheme for articulated robot arms with elastic joints due to reduction gears. This scheme provides a practical solution for sophisticated motion control of general industrial robots using motor-side measurements only. We previously proposed a torsion-angular velocity feedback (TVFB) scheme for suppressing residual vibration in the tip of a 2-DOF robot arm, using a physically parameterized nonlinear observer. To execute exact trajectory control, we also combined a feedforward scheme based on a rigid-joint model with TVFB, due to the complexity of implementing feedforward based on an elastic-joint model. TVFB suppressed arm-tip vibrations caused by feedforward mismatch between the rigid- and elastic-joint models. In this paper, we extend the scope of the combined scheme to a 6-DOF industrial robot. We implement a real-time controller with complete direct and inverse dynamic models for the feedback and feedforward. The effectiveness of our approach was successfully validated in several experiments.

Keywords: Robot arms, Multivariable systems, Mechanical resonance, Vibration suppression, Gray-box modeling, Nonlinear identification, Nonlinear optimization, Nonlinear observer.

1. INTRODUCTION

Articulated robot arms are increasingly expected to improve productivity in the manufacturing, logistics, and service industries. This requires a fast and exact trajectory control scheme that can suppress residual vibrations in the tip of the robot arm. Such vibrations are due to the elasticity of reduction gears in motor-actuated joints. Elasticity in general industrial robots must be controlled by motor-side measurements only, without using link-side measurements.

Many studies of feedforward and feedback schemes have been devoted to motion control of robot arms with joint elasticity (Deluca (2016)). In feedforward schemes, only approximate inverse elastic-joint models can be implemented, because of the presence of gear-damping coefficients (Deluca (2000)). Such schemes also require high-order reference trajectories exceeding the second derivative. With feedback schemes, it is hard to design a general nonlinear observer for estimating link-side variables from motor-side measurements only (Spong (1987)). Thus, approximation schemes with considerable engineering costs have been proposed, such as an extended Kalman filter (Lightcap (2010)) and a singular perturbation method (Kim (2019)).

To solve this problem without such approximations, we proposed a torsion-angular velocity feedback (TVFB) scheme for suppressing residual vibration using motor-side measurements only (Oaki (2015)). This scheme utilizes a simple nonlinear observer based on a physically parameterized dynamic model of a robot arm with elastic harmonic-drive (HD) gears. Although the capability of this observer depends on the identification accuracy of the elastic-joint model, TVFB can be easily plugged into existing individual joint servos. We also combined a feedforward scheme based on a rigid-joint model with TVFB to execute exact trajectories, since implementation of a feedforward scheme based on an elastic-joint model has complexity due to the non-collocation and absence of link-side measurements (Deluca (2000), Deluca (2016)). In rapidly accelerated/decelerated narrow-range point-to-point (PTP) movements, TVFB successfully suppressed arm-tip vibrations in a 2-DOF robot arm that were caused by feedforward mismatch between the rigid- and elastic-joint models (Oaki (2018)). The combined control scheme is simple, and suitable for implementation in general industrial robots using motor-side measurements only.

In this paper, we extend the scope of the combined control scheme to a 6-DOF industrial robot. The rigid- and elastic-joint models are built according to our physical-parameter estimation method, based on both linear and nonlinear least squares using motor-side measurements only (Oaki (2018)). We implement a real-time controller with complete direct and inverse dynamic models for the feedback and feedforward, and conduct several experiments using rapid PTP and continuous-path (CP) movements to validate the effectiveness of our approach.

2. 6-DOF INDUSTRIAL ROBOT CONFIGURATION

Fig. 1 shows the 6-DOF industrial robot (TV800; Toshiba Machine Co., Ltd.). The first, fourth, and fifth joints of the robot are driven by an AC servo motor with an HD

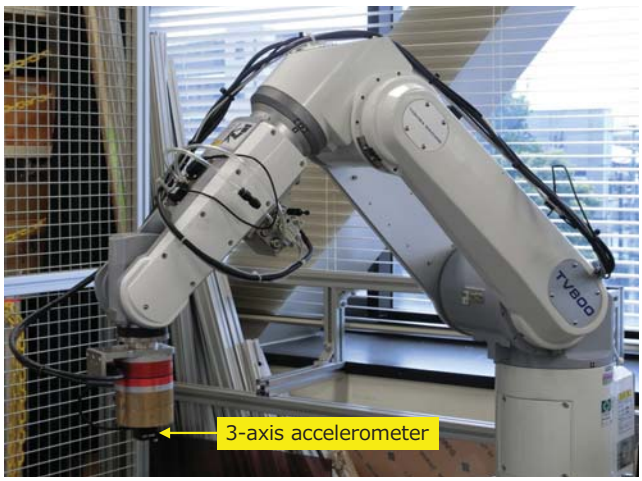

Fig. 1. TV800, a 6-DOF industrial robot. The 3-axis accelerometer is utilized only for monitoring controller performance.

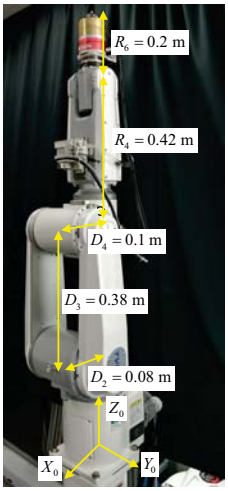

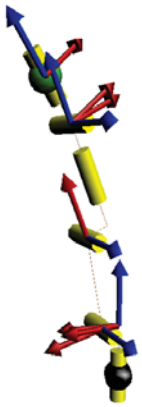

j	γ	α	d	θ	r
1	0	0	0	θ_{L1}	0
2	0	$-\frac{\pi}{2}$	D_2	θ_{L2}	0
3	$-\frac{\pi}{2}$	0	D_3	θ_{L3}	0
4	$-\frac{\pi}{2}$	$-\frac{\pi}{2}$	D_4	θ_{L4}	R_4
5	0	$\frac{\pi}{2}$	0	θ_{L5}	0
6	0	$-\frac{\pi}{2}$	0	θ_{L6}	R_6

Fig. 2. Geometric parameters for the TV800 robot, as defined by the OpenSYMORO software package (Khalil (2014)).

gear via a timing belt. The second, third, and sixth joints are driven by the AC servo motor with the HD gear only. The robot has elastic joints due to the reduction gears. A 2.5 kg payload with a 3-axis accelerometer is attached at the sixth joint. The accelerometer is only utilized for monitoring controller performance. The translation velocity and position of the arm-tip of the robot can be computed by complementary filters using the accelerometer and motor encoders. Fig. 2 shows the geometric parameters for the TV800 robot, defined by the software package OpenSYMORO (Khalil (2014)) (SYMORO, below), an open-source version of SYMORO+ (Khalil (1997)). We also utilize SYMORO to build the dynamic identification model, direct-dynamic model, and inverse-dynamic model for the 6-DOF TV800 robot, which is described below. A computer running the Linux operating system is utilized for real-time robot control and data collection.

3. RIGID- AND ELASTIC-JOINT MODELING

3.1 Frequency response identification of each joint

For initial 6-DOF robot modeling, we performed identification experiments to investigate the mechanical reso-

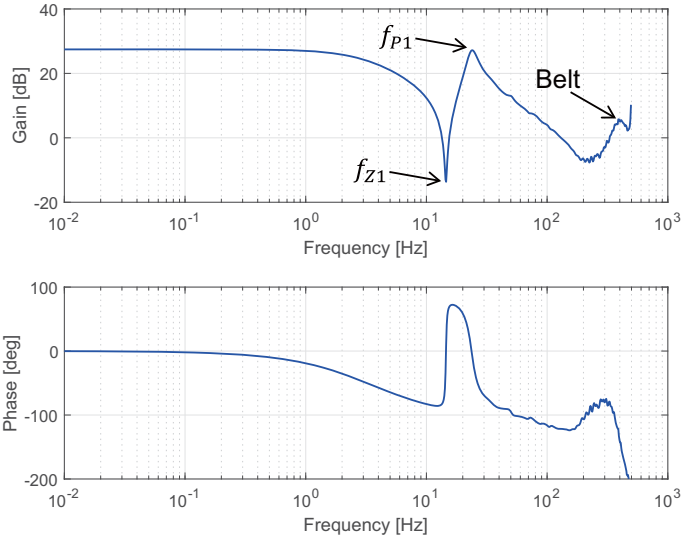

Fig. 3. Estimated FRF from first-joint motor input to motor angular velocity using the high-order ARX model as nonparametric system identification.

nances of each joint, which cause residual vibrations, in the same manner as Oaki (2018). We applied a pseudorandom binary signal to the first joint by open-loop control as motor current reference input data for identification. To produce maximum inertia of the first joint, the second joint is motor-braked at 90 deg, and the four remaining joints are motor-braked at 0 deg. Fig. 3 shows the estimated frequency response function (FRF) of the first joint, which is from its motor current reference input to motor angular velocity, using the least-squares method with the single-input-single-output (SISO) high-order (60th) ARX model as nonparametric system identification. The FRF demonstrates a typical second-order mechanical resonance composed of the anti-resonance frequency f_{Z1} (= 14 Hz) and the resonance frequency f_{P1} (= 22 Hz), which are due to the HD gear in the first joint. Another mechanical resonance peak is estimated at 400 Hz, which is due to the timing belt in the first joint. We can regard the model of the first joint as a two-inertia system because of the 400 Hz resonance peak located at a sufficiently high frequency.

In a similar manner, Figs. 4(a), (b), and (c) show estimated FRFs of the second, third, and fifth joints, respectively. Fig. 4(a) shows a typical second-order mechanical resonance composed of the anti-resonance frequency f_{Z2} (= 11 Hz) and the resonance frequency f_{P2} (= 19 Hz), which are due to the HD gear of the second joint. Fig. 4(b) shows the same anti-resonance frequency f_{Z2} as in Fig. 4(a), and Fig. 4(c) shows the same anti-resonance frequencies f_{Z2} and f_{Z3} (= 32 Hz) as in Fig. 4(b), with f_{Z5} (=55 Hz). These mechanical resonances demonstrate coupled vibrations (Oaki (2018)) among the second, third, and fifth joints. We can thus also regard each model for the second and third joints as a two-inertia system. However, Fig. 4(c) shows another mechanical resonance peak at 110 Hz, which is due to the timing belt in the fifth joint. We thus plugged the first-order low-pass filter with cut-off frequency 100 Hz into the fifth motor current reference so that the fifth-joint model is regarded as a two-inertia system. Although figures for the estimated FRFs in the fourth and sixth joints are omitted due to space limitations, these two joints can also be regarded as two-inertia systems.

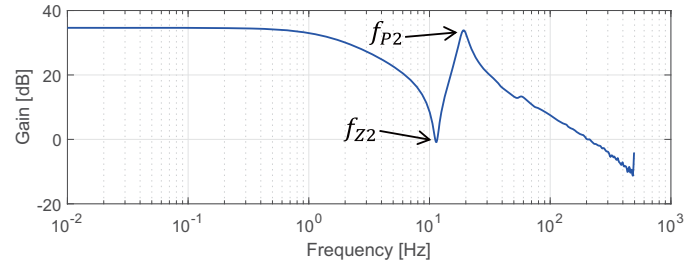

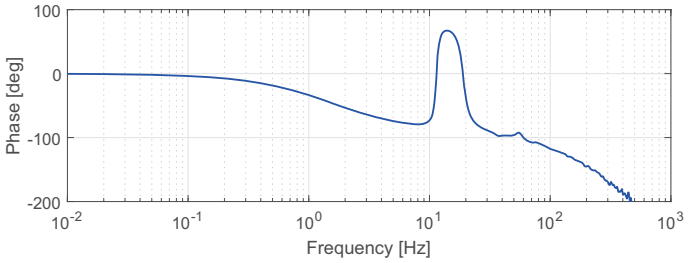

(a) Second joint

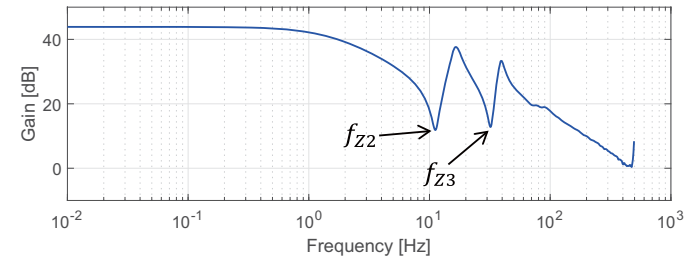

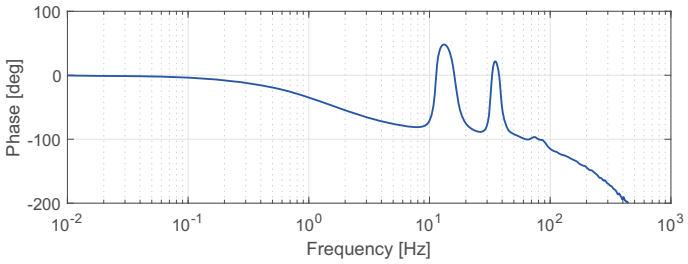

(b) Third joint

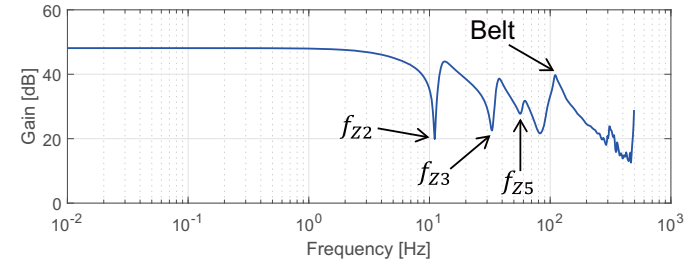

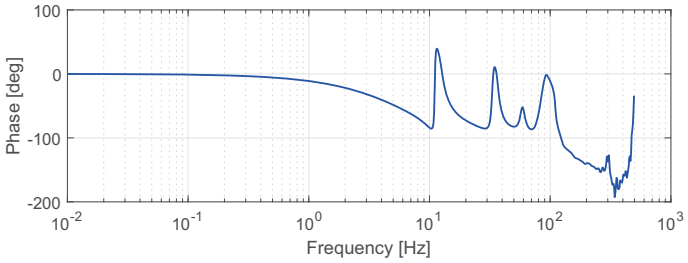

(c) Fifth joint

Fig. 4. Estimated FRFs from each motor input to motor angular velocity using the ARX model.

3.2 Building rigid- and elastic-joint models

From the investigation in the previous subsection, the 6-DOF robot can be modeled as six serially connected two-inertia models. Each two-inertia model is linear and consists of seven physical parameters: the motor-side inertia, link-side inertia, gear-spring coefficient, motor-side viscous-friction coefficient, link-side viscous-friction coefficient, gear-damping coefficient, and motor-side Coulomb-friction torque (Oaki (2015)).

We combine the six two-inertia models with a well-known nonlinear rigid-joint robot model. Then, the elastic-joint model for the 6-DOF robot is given by

$$\begin{aligned}\boldsymbol{M}_M\ddot{\boldsymbol{\theta}}_M + \boldsymbol{D}_M\dot{\boldsymbol{\theta}}_M + \boldsymbol{f}_M\mathrm{sgn}(\dot{\boldsymbol{\theta}}_M) \\ = \boldsymbol{E}\boldsymbol{u} - \boldsymbol{N}_G[\boldsymbol{K}_G(\boldsymbol{N}_G\boldsymbol{\theta}_M - \boldsymbol{\theta}_L) \\ + \boldsymbol{D}_G(\boldsymbol{N}_G\dot{\boldsymbol{\theta}}_M - \dot{\boldsymbol{\theta}}_L)]\end{aligned} \tag{1}$$

$$\begin{aligned}\boldsymbol{M}_L(\boldsymbol{\theta}_L)\ddot{\boldsymbol{\theta}}_L + \boldsymbol{c}_L(\dot{\boldsymbol{\theta}}_L,\boldsymbol{\theta}_L) + \boldsymbol{g}_L(\boldsymbol{\theta}_L) + \boldsymbol{D}_L\dot{\boldsymbol{\theta}}_L \\ = \boldsymbol{K}_G(\boldsymbol{N}_G\boldsymbol{\theta}_M - \boldsymbol{\theta}_L) + \boldsymbol{D}_G(\boldsymbol{N}_G\dot{\boldsymbol{\theta}}_M - \dot{\boldsymbol{\theta}}_L),\end{aligned} \tag{2}$$

where subscript M means motor-side, subscript L means link-side, and subscript G indicates the elastic gear between the motor and the link. Details of the nomenclature are as follows:

$\boldsymbol{\theta}_M = [\theta_{M1},\cdots,\theta_{M6}]^T$: motor angle ($1,\cdots,6$: joint number)
$\boldsymbol{\theta}_L = [\theta_{L1},\cdots,\theta_{L6}]^T$: link angle
$\boldsymbol{M}_L(\boldsymbol{\theta}_L) \in R^{6\times6}$: link inertia matrix
$\boldsymbol{c}_L(\dot{\boldsymbol{\theta}}_L,\boldsymbol{\theta}_L) \in R^{6\times1}$: Coriolis and centrifugal torque vector
$\boldsymbol{g}_L(\boldsymbol{\theta}_L) \in R^{6\times1}$: gravity torque vector
$\boldsymbol{M}_M = \mathrm{diag}(m_{M1},\cdots,m_{M6})$: motor-side inertia
$\boldsymbol{D}_M = \mathrm{diag}(d_{M1},\cdots,d_{M6})$: motor-side viscous-friction coefficient
$\boldsymbol{D}_L = \mathrm{diag}(d_{L1},\cdots,d_{L6})$: link-side viscous-friction coefficient
$\boldsymbol{K}_G = \mathrm{diag}(k_{G1},\cdots,k_{G6})$: gear-spring coefficient
$\boldsymbol{D}_G = \mathrm{diag}(d_{G1},\cdots,d_{G6})$: gear-damping coefficient
$\boldsymbol{N}_G = \mathrm{diag}(n_{G1},\cdots,n_{G6})$: gear-reduction ratio $(n_{G1},\cdots,n_{G6} \le 1)$
$\boldsymbol{f}_M = [f_{M1},\cdots,f_{M6}]^T$: motor-side Coulomb-friction torque
$\boldsymbol{E} = \mathrm{diag}(e_1,\cdots,e_6)$: torque/input-voltage coefficient
$\boldsymbol{u} = [u_1,\cdots,u_6]^T$: input voltage (motor current control reference).

The elastic-joint models (1) and (2) are essentially derived based on Spong's assumptions (Spong (1987)). Since we employ rich friction and damping parameters, the models are in better agreement with the acquired robot data. $\boldsymbol{M}_L(\boldsymbol{\theta}_L)$, $\boldsymbol{c}_L(\dot{\boldsymbol{\theta}}_L,\boldsymbol{\theta}_L)$, and $\boldsymbol{g}_L(\boldsymbol{\theta}_L)$ can be described using the base inertial parameters, which are built by combining each mass, inertia, center-of-mass, and link lengths for the robot. The base inertial and friction parameters for the rigid-joint model are known to be identifiable using robot motion data (Khalil (2002)).

We also define the rigid-joint model below the mechanical resonance frequency using the approximation $\boldsymbol{\theta}_M = \boldsymbol{N}_G^{-1}\boldsymbol{\theta}_L$ in (1) and (2) as

$$\begin{aligned}\boldsymbol{M}(\boldsymbol{\theta}_L)\ddot{\boldsymbol{\theta}}_L + \boldsymbol{c}_L(\dot{\boldsymbol{\theta}}_L,\boldsymbol{\theta}_L) + \boldsymbol{g}_L(\boldsymbol{\theta}_L) + \boldsymbol{D}\dot{\boldsymbol{\theta}}_L \\ + \boldsymbol{N}_G^{-1}\boldsymbol{f}_M\mathrm{sgn}(\dot{\boldsymbol{\theta}}_M) = \boldsymbol{N}_G^{-1}\boldsymbol{E}\boldsymbol{u}\end{aligned} \tag{3}$$

$$\boldsymbol{M}(\boldsymbol{\theta}_L) = \boldsymbol{M}_L(\boldsymbol{\theta}_L) + \mathrm{diag}(m_{M1}/n_{G1}^2,\cdots,m_{M6}/n_{G6}^2) \tag{4}$$

$$\boldsymbol{D} = \mathrm{diag}(d_{L1} + d_{M1}/n_{G1}^2,\cdots,d_{L6} + d_{M6}/n_{G6}^2). \tag{5}$$

The base inertial and friction parameters can be obtained using the dynamic identification model function of SYMORO as follows:

Combined inertia:

First joint: $ZZR1$

Second joint: $XXR2, ZZR2, MX2, MYR2$

Third joint: $XXR3, ZZR3, MXR3, MYR3$

Fourth joint: $XXR4, ZZR4, MX4, MYR4$

Fifth joint: $XXR5, ZZR5, MX5, MYR5$

Sixth joint: $XXR6, ZZ6, MX6, MY6$

Motor-side inertia:

$IA3, IA4, IA5, IA6 \equiv m_{Mi}/n_{Gi}^2$ $(i = 3, \cdots, 6)$

Viscous friction coefficient:

$FV1, FV2, FV3, FV4, FV5, FV6 \equiv d_{Li} + d_{Mi}/n_{Gi}^2$ $(i = 1, \cdots, 6)$

Coulomb friction torque:

$FS1, FS2, FS3, FS4, FS5, FS6 \equiv f_{M1}/n_{Gi}^2$ $(i = 1, \cdots, 6)$.

Note that the motor-side inertias $IA1$ and $IA2$ must be estimated for the elastic-joint model. Also, the viscous friction coefficients must be separated into the motor side.

3.3 Basic independent joint servos

Basic independent joint servos for the robot are follows:

$$u_i = k_{PVi}\,[k_{FVi}\,v_{MRi} + \frac{1}{t_{IVi}}\int (v_{MRi} - \dot{\theta}_{Mi})\,dt - \dot{\theta}_{Mi}]$$
$$v_{MRi} = k_{PPi}\,(\theta_{MRi} - \theta_{Mi}), \tag{6}$$

where

θ_{MRi}: Motor-angle position reference (i=1,$\cdots$,6: joint number)
θ_{Mi}: Motor angle
k_{PPi}: Proportional feedback gain of motor-angle position
v_{MRi}: Motor angular velocity reference
$\dot{\theta}_{Mi}$: Motor angular velocity
k_{FVi}: Feedforward gain of motor angular velocity reference
t_{IVi}: Time constant of integral of motor angular velocity error
k_{PVi}: Proportional feedback gain of motor angular velocity
u_i: Input voltage (motor current control reference)

Each 2-DOF PI (feedforward–integral–proportional (FF–I–P)) velocity-control loop is stably tuned using the frequency domain (Oaki (2015)), which is connected with an outer-P (proportional) position-control loop.

Joint servos can be utilized to perform movements for estimation of physical parameters, as described below.

3.4 Physical parameter estimation for the 6-DOF robot

The following summarizes the physical parameter estimation procedure, composed of four steps (Oaki (2018)).

Step 1: Estimate mechanical resonance frequencies

Mechanical resonance frequencies in each joint can be estimated using the SISO ARX modeling.

Step 2: Estimate ase parameter for the rigid-joint model

Properly excited movement data for each joint are acquired and resampled at below the mechanical resonance frequencies. The base inertial and friction parameters can be estimated by the linear least-squares method using a regressor matrix built with resampled data.

Step 3: Estimate initial parameter for elastic-joint model

Physical parameters for each two-inertia model are initially estimated. The motor-side inertias ($IA1$, $IA2$) and gear-spring coefficients $(k_{G1}, \cdots, k_{G6})$ can be tentatively calculated using the mechanical resonance frequencies and the maximum inertia of each diagonal component of $\boldsymbol{M}(\boldsymbol{\theta}_L)$ (Oaki (2018)). However, the $\boldsymbol{D}_M$, $\boldsymbol{D}_L$, and $\boldsymbol{D}_G$ cannot be separately calculated. Tentative values are thus set using the viscous friction coefficients for the rigid-joint model, for example, $d_{M1}/n_{G1}^2 = d_{L1} = d_{G1} = 0.5FV1$.

Step 4: Nonlinear optimization using velocity step response

The closed-loop simulator is built based on elastic-joint models (1) and (2), and the motor velocity controllers (6) with the physical parameters initially estimated above. The 6-DOF robot simulator can be implemented thanks to the direct-dynamic model function in SYMORO.

The nonlinear least-squares estimation method (Mathworks (2018)) is performed using motor velocity step-response data from the actual robot and model simulations. An evaluation function E_V based on the squared-error norm using the motor angular velocity and the motor current reference was adopted as

$$E_V = \int (r\,\Delta\dot{\boldsymbol{\theta}}_M^2 + \Delta\boldsymbol{u}^2)\,dt, \tag{7}$$

where r is a weight ratio for better optimization tuning. Note that this nonlinear optimization is performed using only motor-side measurements.

4. COMBINED CONTROL SCHEME

Fig. 5 shows the basic independent joint servos with TVFB based on the elastic-joint model $\boldsymbol{\tau}_{TVFB}$, feedforward compensation of the feedback delay of the PI controller $\boldsymbol{\tau}_{FF1}$, and feedforward based on the rigid-joint model $\boldsymbol{\tau}_{FF2}$. (Oaki (2018)).

4.1 Residual vibration suppression using TVFB

The TVFB scheme consists of a nonlinear state observer to increase damping effects without redesigning existing velocity controllers for the basic joint servos (Oaki (2015)). The nonlinear state observer is based on the physically parameterized dynamic model with the PI velocity feedback. The PI gains are set to be identical to those of the existing motor velocity controllers. The twice-differentiated nonlinear observer dynamics are given by

$$\ddot{\hat{\boldsymbol{\theta}}}_M = \boldsymbol{M}_M^{-1}\{-\boldsymbol{D}_M\dot{\hat{\boldsymbol{\theta}}}_M - \boldsymbol{f}_M\mathrm{sgn}(\dot{\hat{\boldsymbol{\theta}}}_M) + \boldsymbol{E}\boldsymbol{\tau} - \boldsymbol{N}_G[\boldsymbol{K}_G(\boldsymbol{N}_G\hat{\boldsymbol{\theta}}_M - \hat{\boldsymbol{\theta}}_L) + \boldsymbol{D}_G(\boldsymbol{N}_G\dot{\hat{\boldsymbol{\theta}}}_M - \dot{\hat{\boldsymbol{\theta}}}_L)]\} \tag{8}$$

$$\ddot{\hat{\boldsymbol{\theta}}}_L = \boldsymbol{M}_L(\hat{\boldsymbol{\theta}}_L)^{-1}[-\boldsymbol{c}_L(\dot{\hat{\boldsymbol{\theta}}}_L, \hat{\boldsymbol{\theta}}_L) - \boldsymbol{D}_L\dot{\hat{\boldsymbol{\theta}}}_L + \boldsymbol{K}_G(\boldsymbol{N}_G\hat{\boldsymbol{\theta}}_M - \hat{\boldsymbol{\theta}}_L) + \boldsymbol{D}_G(\boldsymbol{N}_G\dot{\hat{\boldsymbol{\theta}}}_M - \dot{\hat{\boldsymbol{\theta}}}_L)] \tag{9}$$

$$\boldsymbol{\tau} = \boldsymbol{K}_{PV}\,[(\dot{\boldsymbol{\theta}}_M - \dot{\hat{\boldsymbol{\theta}}}_M) + \boldsymbol{t}_{IV}{}^{-1}\int (\dot{\boldsymbol{\theta}}_M - \dot{\hat{\boldsymbol{\theta}}}_M)\,dt] + \boldsymbol{u}\,, \tag{10}$$

with the following parameters:

$\hat{}$: State variable estimated by observer
$\dot{\boldsymbol{\theta}}_M = [\dot{\theta}_{M1}, \cdots, \dot{\theta}_{M6}]^T$: Motor angular velocity input to observer
$\boldsymbol{u} = [u_1, \cdots, u_6]^T$: Motor current reference input to observer
$\boldsymbol{K}_{PV} = \mathrm{diag}(k_{PV1}, \cdots, k_{PV6})$: Proportional feedback gain
$\boldsymbol{t}_{IV} = \mathrm{diag}(t_{IV1}, \cdots, t_{IV6})$: Time constant of integral feedback
$\boldsymbol{\tau} = [\tau_1, \cdots, \tau_6]^T$: Motor current reference input in the observer.

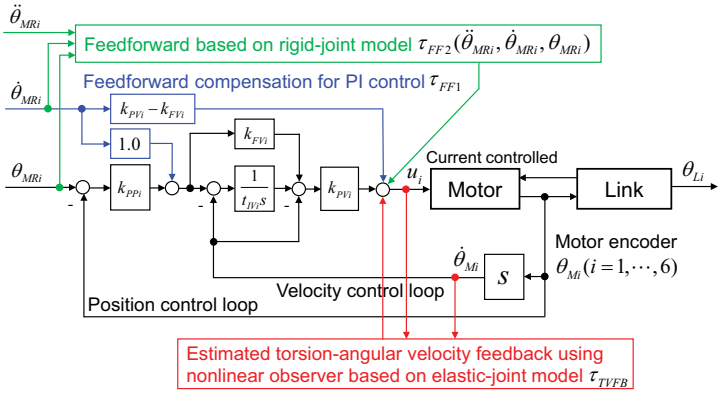

Fig. 5. Basic independent joint servos with TVFB based on the elastic-joint model $\boldsymbol{\tau}_{TVFB}$, feedforward compensation for feedback delay of the PI controller $\boldsymbol{\tau}_{FF1}$, and feedforward based on the rigid-joint model $\boldsymbol{\tau}_{FF2}$.

The low-pass filter, mentioned above, is also plugged into the fifth motor current reference in the observer. The physically parameterized observer can be also implemented using the direct-dynamic model function in SYMORO.

TVFB τ_{TVFB} is given by

$$\boldsymbol{\tau}_{TVFB} = -\operatorname{diag}(k_{TV1}(\hat{\dot{\theta}}_{L1}/n_{G1} - \hat{\dot{\theta}}_{M1}), \cdots, k_{TV6}(\hat{\dot{\theta}}_{L6}/n_{G6} - \hat{\dot{\theta}}_{M6})), \quad (11)$$

where k_{TVi} is the TVFB gain in each joint, which can easily be hand-tuned to increase damping of the velocity-step response. A gain-scheduled TVFB scheme for arm-posture changing (Oaki (2015)) is not required here, because a payload of only 2.5 kg is handled.

4.2 Feedforward to execute exact trajectory

The feedforward τ_{FF} consists of two terms:

$$\boldsymbol{\tau}_{FF} = \boldsymbol{K}_{IV} \int \dot{\boldsymbol{\theta}}_{MR}\, dt + (\boldsymbol{K}_{PV} - \boldsymbol{K}_{FV})\, \dot{\boldsymbol{\theta}}_{MR} + \boldsymbol{E}^{-1}[\boldsymbol{M}(\boldsymbol{\theta}_{MR})\ddot{\boldsymbol{\theta}}_{MR} + \boldsymbol{c}(\dot{\boldsymbol{\theta}}_{MR}, \boldsymbol{\theta}_{MR}) + \boldsymbol{D}\,\dot{\boldsymbol{\theta}}_{MR} + \boldsymbol{f}_M \operatorname{sgn}(\dot{\boldsymbol{\theta}}_{MR})], \quad (12)$$

where $\dot{\boldsymbol{\theta}}_{MR}$ and $\ddot{\boldsymbol{\theta}}_{MR}$ are the motor angular velocity and motor angular acceleration references. The first term compensates for feedback delay of the PI controller in the basic joint servos. The second term is feedforward based on the rigid-joint model for executing exact trajectory control. The feedforward based on the rigid-joint model can be implemented using the inverse-dynamic model function in SYMORO.

5. EXPERIMENTAL RESULTS AND DISCUSSION

We tuned the basic independent joint servos (6) for the TV800 6-DOF robot with a 2.5 kg payload in the frequency domain. All experiments below were performed at 0.25 ms control intervals.

5.1 Model parameter estimation and TVFB gain tuning

We first obtained the mechanical resonance frequencies f_{Z1}, f_{P1}, etc., using the estimated FRFs.

We next conducted properly excited movements for estimating the 25 base inertial and 12 friction parameters. Movement data were resampled at 25 ms. Table 1 shows estimated base parameters for the rigid-joint model, and Table 2 shows system and control parameters.

We then calculated the initial elastic-joint model parameters and performed nonlinear optimization. The weight ratio r was tuned and set to 0.1 in (7). Table 3 shows the estimated physical parameters. Note that the 15 base inertial parameters, marked "←" in Table 3, were already well estimated and thus did not require optimization. Optimization for the 42 physical parameters took less than three minutes on a computer with a Core-i7 (4-core) CPU.

Figs. 6(a) and (b) demonstrate velocity step/disturbance response examples for comparison between the actual robot and the model with optimized physical parameters, using only the FF–I–P velocity controller. The good agreements of the motor angular velocities and motor current references demonstrates the estimated model accuracy.

Figs. 7(a) and (b) show that the TVFB gains $k_{TV1,2}$ are easily hand-tuned using the step response of the link-angular velocity estimated by the nonlinear state observer. Also, Figs. 7(c) and (d) demonstrate that the TVFB gain k_{TV2} allows $k_{TV3,5}$ to be set to 0, thanks to the feedback scheme based on the 6-DOF elastic-joint model.

5.2 Performance evaluation of the combined controller

The combined controller for the 6-DOF robot was implemented using the estimated rigid- and elastic-joint models. We conducted several experiments using PTP and CP movements to validate the effectiveness of the controller.

Fig. 8 shows a rapidly accelerated/decelerated narrow-range PTP reciprocal movement pattern between two $\boldsymbol{\theta}_L$ points, $[0, 90, 0, 0, 0, 0]^T$ and $[5, 95, 5, 5, 5, 5]^T$ [deg]for evaluating positioning performance.

Figs. 9(a), (b), and (c) show comparisons of motor current references for the first, second, and third joints with and without TVFB. These figures also show each component of the feedforward based on the rigid-joint model in the motor current references. The small differences between the feedforward and motor current references demonstrate the accuracy of the rigid-joint model. TVFB suppresses residual vibrations of the motor current references, caused by feedforward mismatch between the rigid- and elastic-joint models. Fig. 10 compares residual vibration at the arm-tip position in the vertical direction with and without TVFB. The solid lines show the link (arm-tip) position using the accelerometer, the dashed lines show the virtual motor position calculated using the motor angular position and gear-reduction ratios, and the dot-dash lines show the arm-tip position reference trajectory. This figure clearly shows that control using feedforward with TVFB can satisfy both exact execution of trajectories and suppression of residual vibrations.

Figs. 11 and 12 show a rapid 0.2 m square CP movement pattern parallel to the X_0–Y_0 plane with vertical-downward orientation of the arm tip. Figs. 13, 14, and 15 also show that the feedforward based on the rigid-joint model in combination with TVFB based on the elastic-joint model can realize accurate and stable motion during highly nonlinear cornering movements.

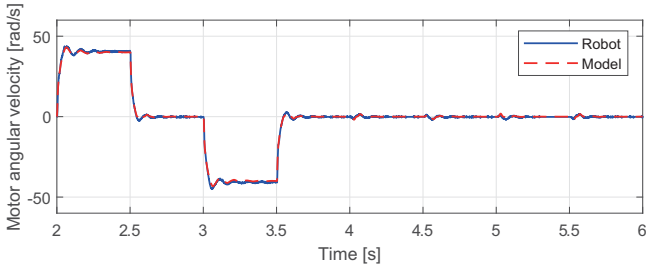

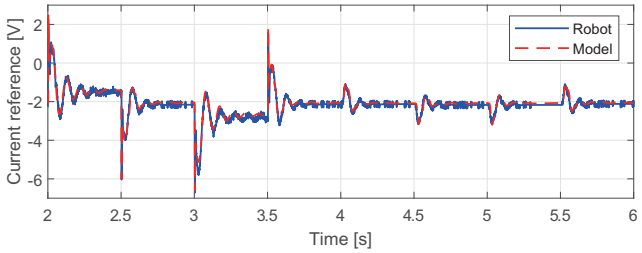

(a) Second motor angular velocity and motor current reference

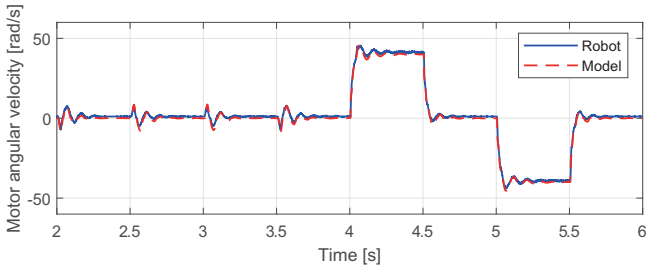

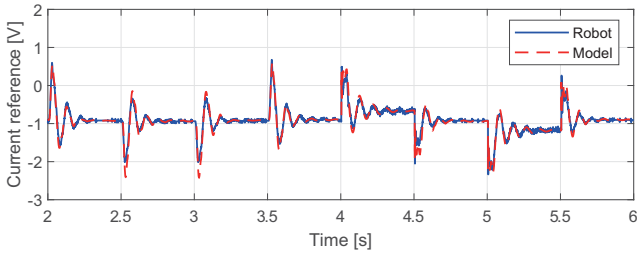

(b) Third motor angular velocity and motor current reference

Fig. 6. Velocity step response comparisons between actual robot and model using optimized physical parameters.

Table 1. Rigid-joint model parameters estimated using the linear least-squares method.

$ZZR1$ [kgm^2]	5.13e+00
$XXR2$ [kgm^2]	2.40e+00
$ZZR2$ [kgm^2]	5.33e+00
$MXR2$ [kgm^2]	1.62e-01
$MYR2$ [kgm^2]	-5.44e+00
$XXR3$ [kgm^2]	-7.98e-01
$ZZR3$ [kgm^2]	1.18e+00
$MXR3$ [kgm^2]	2.22e+00
$MYR3$ [kgm^2]	-8.19e-01
$XXR4$ [kgm^2]	6.05e-02
$ZZR4$ [kgm^2]	8.11e-02
$MX4$ [kgm^2]	2.11e-02
$MYR4$ [kgm^2]	-4.48e-03
$XXR5$ [kgm^2]	-1.52e-01
$ZZR5$ [kgm^2]	4.43e-02
$MX5$ [kgm^2]	-6.06e-03
$MYR5$ [kgm^2]	3.72e-01
$XXR6$ [kgm^2]	-2.43e-04
$ZZ6$ [kgm^2]	5.16e-02
$MX6$ [kgm^2]	-5.86e-04
$MY6$ [kgm^2]	1.26e-02

$IA3$ [kgm^2]	5.01e-01
$IA4$ [kgm^2]	5.42e-01
$IA5$ [kgm^2]	6.93e-02
$IA6$ [kgm^2]	1.32e-01
$FV1$ [Nms/rad]	2.05e+01
$FV2$ [Nms/rad]	1.45e+01
$FV3$ [Nms/rad]	3.07e+00
$FV4$ [Nms/rad]	5.30e+00
$FV5$ [Nms/rad]	6.61e-01
$FV6$ [Nms/rad]	2.52e-01
$FS1$ [Nm]	3.08e+01
$FS2$ [Nm]	1.79e+01
$FS3$ [Nm]	4.70e+00
$FS4$ [Nm]	9.17e+00
$FS5$ [Nm]	1.89e+00
$FS6$ [Nm]	7.52e-01

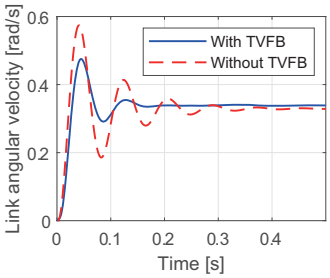

(a) First joint ($k_{TV1} = 0.135$)

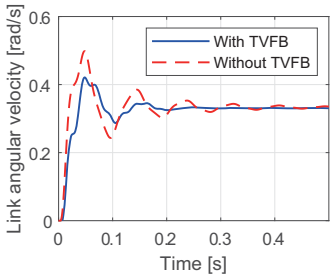

(b) Second joint ($k_{TV2} = 0.180$)

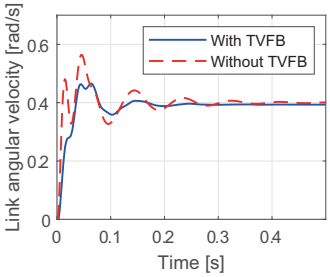

(c) Third joint ($k_{TV3} = 0.0$)

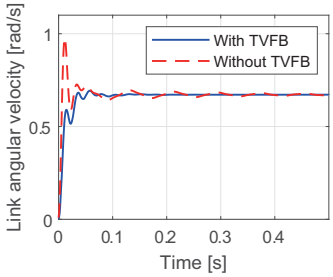

(d) Fifth joint ($k_{TV5} = 0.0$)

Fig. 7. TVFB gains $k_{TV1,2}$ were easily hand-tuned using velocity step responses. $k_{TV3,\cdots,6}$ were set to 0 thanks to the feedback scheme based on a 6-DOF elastic-joint model.

Table 2. System and control parameters.

System parameters	
e_1 [Nm/V]	0.318
e_2 [Nm/V]	0.318
e_3 [Nm/V]	0.283
e_4 [Nm/V]	0.226
e_5 [Nm/V]	0.226
e_6 [Nm/V]	0.219
n_{G1}	1/121.5
n_{G2}	1/120
n_{G3}	1/100
n_{G4}	1/82.1667
n_{G5}	1/59.5
n_{G6}	1/50

Velocity controller gains	
k_{FV1-6}	0.30
t_{IV1-6} [s]	0.015
k_{PV1}	0.36
k_{PV2}	0.36
k_{PV3}	0.10
k_{PV4}	0.10
k_{PV5}	0.05
k_{PV6}	0.02
Position controller gains	
k_{PP1-6} [rad/s]	20.0
TVFB gains	
k_{TV1}	0.135
k_{TV2}	0.180
k_{TV3-6}	0.000

6. CONCLUSION

We extended the scope of our combined control scheme to a 6-DOF industrial robot. We implemented a real-time controller with complete direct and inverse dynamic models for feedback and feedforward. Several experiments successfully validated the effectiveness of our approach.

Further studies include a formal stability analysis. The original idea of our combined control scheme depends on the identification accuracy of the rigid- and elastic-joint models. Careful identification work helps the control scheme not to occur a stability problem in practical use, and to greatly bring out its capability.

We believe that the proposed combined controller provides a practical solution for sophisticated motion control of general industrial robot arms with joint elasticity due to reduction gears.

Table 3. Estimated elastic-joint model parameters using nonlinear optimization.

	Before opt.	After opt.
$ZZR1$ [kgm^2]	2.57e+00	1.06e+00
$XXR2$ [kgm^2]	2.40e+00	⟵
$ZZR2$ [kgm^2]	2.66e+00	2.06e+00
$MXR2$ [kgm^2]	1.62e-01	⟵
$MYR2$ [kgm^2]	-5.44e+00	⟵
$XXR3$ [kgm^2]	-7.98e-01	⟵
$ZZR3$ [kgm^2]	1.18e+00	9.67e-01
$MXR3$ [kgm^2]	2.22e+00	⟵
$MYR3$ [kgm^2]	-8.19e-01	⟵
$XXR4$ [kgm^2]	6.05e-02	⟵
$ZZR4$ [kgm^2]	8.11e-02	2.02e-02
$MX4$ [kgm^2]	2.11e-02	⟵
$MYR4$ [kgm^2]	-4.48e-03	⟵
$XXR5$ [kgm^2]	-1.52e-01	⟵
$ZZR5$ [kgm^2]	4.43e-02	9.41e-03
$MX5$ [kgm^2]	-6.06e-03	⟵
$MYR5$ [kgm^2]	3.72e-01	⟵
$XXR6$ [kgm^2]	-2.43e-04	⟵
$ZZ6$ [kgm^2]	5.16e-02	1.31e-02
$MX6$ [kgm^2]	-5.86e-04	⟵
$MY6$ [kgm^2]	1.26e-02	⟵
m_{M1} [kgm^2]	1.74e-04	2.84e-04
m_{M2} [kgm^2]	1.85e-04	2.39e-04
m_{M3} [kgm^2]	5.01e-05	3.68e-05
m_{M4} [kgm^2]	8.03e-05	8.41e-05
m_{M5} [kgm^2]	1.96e-05	1.64e-05
m_{M6} [kgm^2]	5.29e-05	1.31e-05
k_{G1} [Nm/rad]	6.73e+04	5.31e+04
k_{G2} [Nm/rad]	5.72e+04	4.25e+04
k_{G3} [Nm/rad]	3.10e+04	3.30e+04
k_{G4} [Nm/rad]	2.50e+04	2.89e+04
k_{G5} [Nm/rad]	6.74e+03	4.38e+03
k_{G6} [Nm/rad]	3.41e+03	2.18e+03
d_{M1} [Nms/rad]	6.95e-04	1.47e-03
d_{M2} [Nms/rad]	5.04e-04	7.261e-04
d_{M3} [Nms/rad]	1.53e-04	7.43e-04
d_{M4} [Nms/rad]	3.93e-04	2.68e-06
d_{M5} [Nms/rad]	9.34e-05	2.36e-04
d_{M6} [Nms/rad]	5.03e-05	1.35e-04
d_{L1} [Nms/rad]	1.03e+01	2.50e+01
d_{L2} [Nms/rad]	7.26e+00	1.03e+01
d_{L3} [Nms/rad]	1.53e+00	9.99e-01
d_{L4} [Nms/rad]	2.65e+00	2.45e+00
d_{L5} [Nms/rad]	3.31e-01	5.29e-01
d_{L6} [Nms/rad]	1.26e-01	1.21e+00
d_{G1} [Nms/rad]	1.03e+01	2.19e+01
d_{G2} [Nms/rad]	7.26e+00	4.08e+00
d_{G3} [Nms/rad]	1.53e+00	4.44e+00
d_{G4} [Nms/rad]	2.65e+00	1.40e+00
d_{G5} [Nms/rad]	3.31e-01	1.30e-02
d_{G6} [Nms/rad]	1.26e-01	2.61e-01
f_{M1} [Nm]	2.53e-01	1.97e-01
f_{M2} [Nm]	1.49e-01	1.39e-01
f_{M3} [Nm]	4.70e-02	4.31e-02
f_{M4} [Nm]	1.12e-01	1.47e-01
f_{M5} [Nm]	3.18e-02	2.51e-02
f_{M6} [Nm]	1.50e-02	4.97e-03

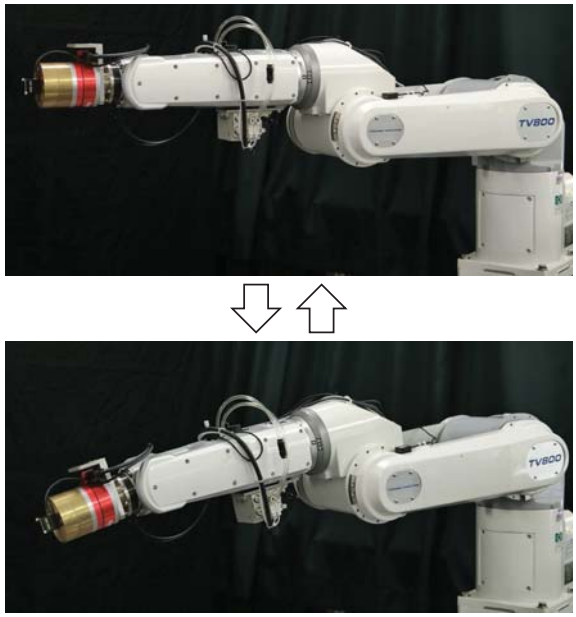

Fig. 8. Rapidly accelerated/decelerated narrow-range PTP reciprocal movement between two $\boldsymbol{\theta}_L$ points, $[0, 90, 0, 0, 0, 0]^T$ and $[5, 95, 5, 5, 5, 5]^T$ [deg].

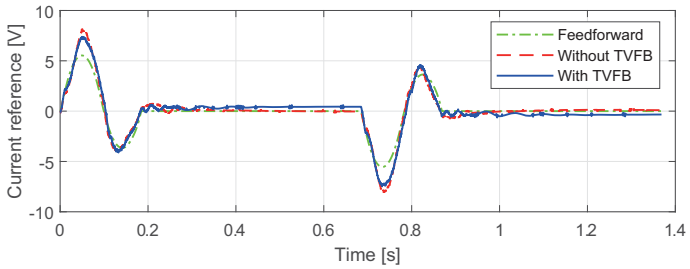

(a) First joint

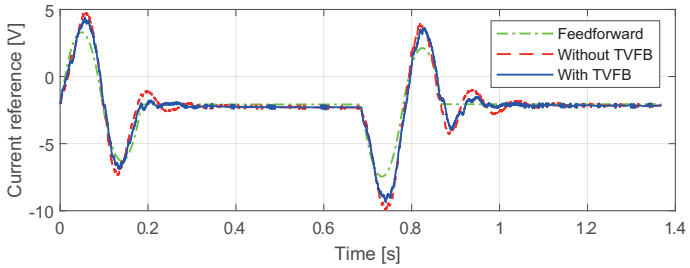

(b) Second joint

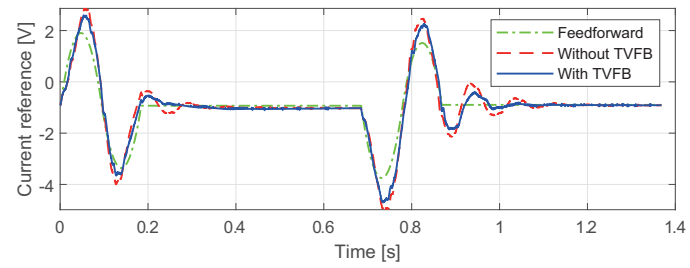

(c) Third joint

Fig. 9. Comparison of motor current references for the first, second, and third joints, with and without TVFB.

REFERENCES

De Luca, A. (2000). Feedforward / feedback laws for the control of flexible robots. *Proc. IEEE International Conference on Robotics and Automation, San Francisco, CA*, 233–240.

De Luca, A., and Book, W. (2016). Robots with flexible elements. in: *Springer Handbook of Robotics, 2nd Edition, Siciliano, B., and Khatib, O. Eds. Springer*, Chapter 11.

Khalil, W., and Creusot, D. (1997). SYMORO+: A system for the symbolic modelling of robots. *Robotica*. 15, 153–161.

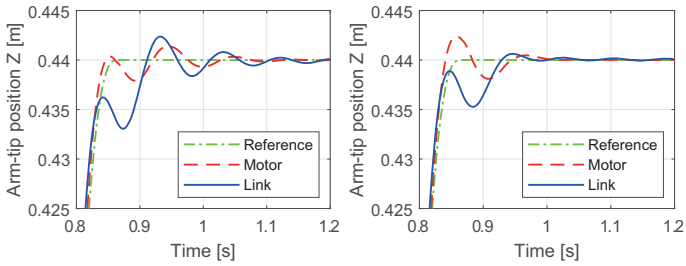

(a) Without TVFB (b) With TVFB

Fig. 10. Comparison of residual vibration of arm-tip positions in vertical direction with and without TVFB.

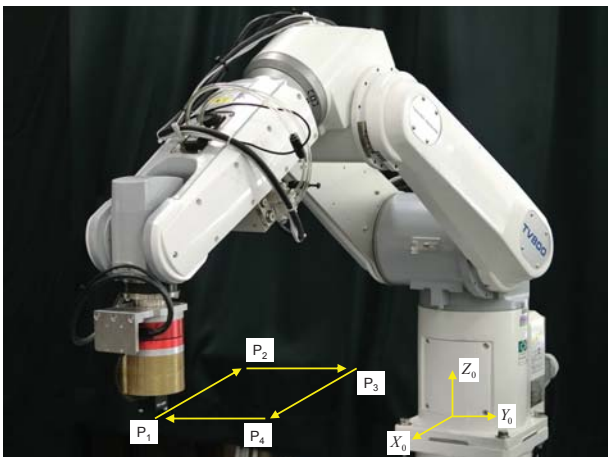

Fig. 11. Rapid 0.2 m square CP movement parallel to the X_0–Y_0 plane with vertical-downward orientation of the arm tip.

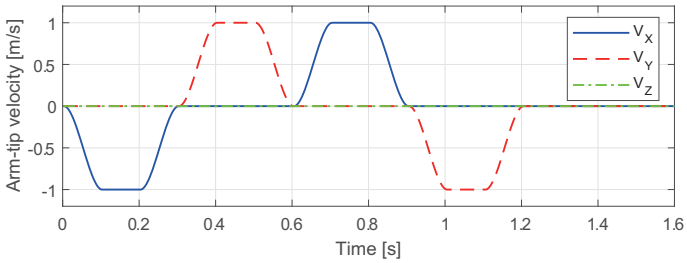

Fig. 12. Velocity references at base coordinates for the rapid 0.2 m square CP movement.

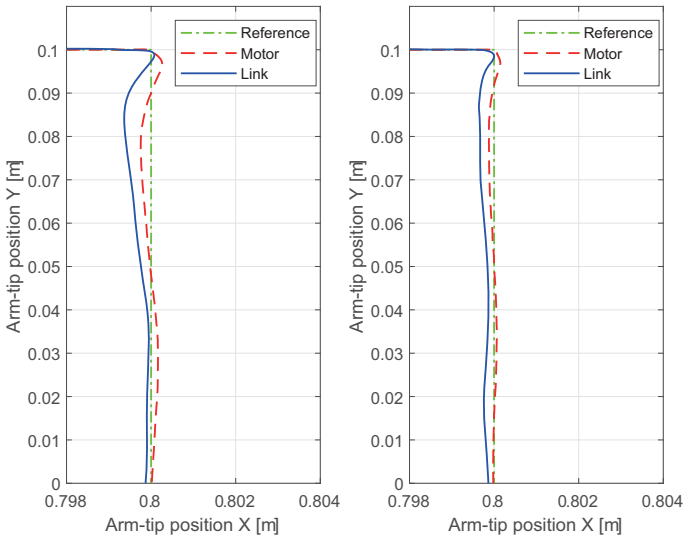

(a) Without TVFB (b) With TVFB

Fig. 13. Comparison of arm-tip position accuracy around corner P4 with and without TVFB.

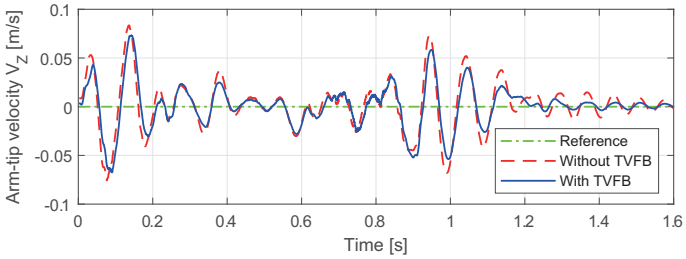

Fig. 14. Comparison of arm-tip velocity in vertical direction during CP movement with and without TVFB.

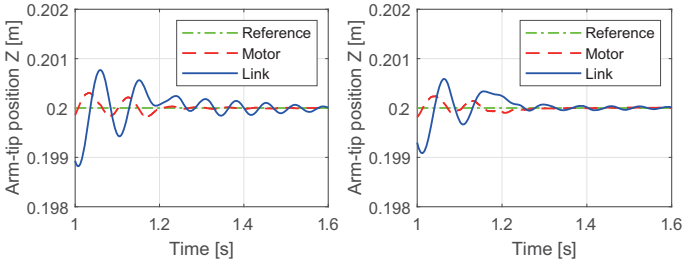

(a) Without TVFB (b) With TVFB

Fig. 15. Comparison of residual vibration at the arm-tip position in the vertical direction at final position P1 with and without TVFB.

Khalil, W., and Dombre, E. (2002). Modeling, Identification & Control of Robots. *Kogan Page Science*.

Khalil, W., Vijayalingam, A., Khomutenko, B., Mukhanov, I., Lemoine, P., and Ecorchard, G. (2014). OpenSYMORO: An open-source software package for Symbolic Modelling of Robots. *Proc. 2014 IEEE/ASME International Conference on Advanced Intelligent Mechatronics, Besançon, France*, 1206–1211.

Kim, J., and Croft, A. (2019). Full-State Tracking Control for Flexible Joint Robots With Singular Perturbation Techniques. *Trans. IEEE Control Systems Technology*, 27(1), 63–73.

Lightcap, C. A., and Banks, S. A. (2010). An Extended Kalman Filter for Real-Time Estimation and Control of a Rigid-Link Flexible-Joint Manipulator. *Trans. IEEE Control Systems Technology*, 18(1), 91–103.

MathWorks. (2018). MATLAB Optimization Toolbox Version 8.2 (2018b). *The MathWorks*.

Oaki, J., and Adachi, S. (2015). Vibration-Suppression and Fast-Positioning Control of Elastic-Joint Robot Arm Utilizing Nonlinear-Model-Based Phase-Lead Compensator. *Proc. 2015 IEEE Conference on Control Applications, Sydney, Australia*, 281–287.

Oaki, J. (2018). Physical Parameter Estimation for Feedforward and Feedback Control of a Robot Arm with Elastic Joints. *IFAC-PapersOnLine*, 51(15), 425–430.

Spong, M.W. (1987). Modeling and Control of Elastic Joint Robots. *Trans. ASME J. Dynamic Systems, Measurement and Control*, 109, 310–319.